Infiltration of porous uranium oxide microspheres prepared by internal gelation

Gamze Colak*;[a,b] Gregory Leinders;[a] Rémi Delville;[a] Frédéric Jutier;[a] Marc Verwerft;[a] Jef Vleugels [b]

[a] Belgian Nuclear Research Centre (SCK CEN), Institute for Nuclear Materials Science, Boeretang 200, B-2400 Mol, Belgium.
[b] KU Leuven, Department of Materials Engineering, Kasteelpark Arenberg 44, B-3001 Leuven, Belgium.

Highlights

- Fabrication of uranium oxide microspheres *via* internal gelation, with and without the use of pore-formers
- Application of different calcination temperatures has a pronounced effect on density and porosity
- Infiltration of porous microspheres with neodymium nitrate solutions
- Single phase $U_{1-y}Nd_yO_{2-x}$ solid solution formation after sintering

Abstract

Process conditions for the fabrication of porous uranium oxide microspheres prepared *via* internal gelation were assessed. To improve conditions for the application of infiltration, microstructural parameters such as density, porosity and specific surface area were assessed. Specifically, the effect of calcination temperature and the use of pore-formers was studied. Accessible porosity levels around 20% were obtained after calcination at 773 K or 823 K, without the use of a pore-former. As a novel application, starch was used as a low-temperature, burnable pore-former, and its effect was compared to that of graphite. Accessible porosity levels increased to 34% after calcination due to the use of starch, whereas the application of graphite was discarded because it requires too elevated calcination temperatures. A subset of porous uranium oxide microspheres was infiltrated with neodymium nitrate solution as a surrogate for americium nitrate. Very good agreement between targeted and actual Nd content was observed after sintering of the microspheres, and a maximum concentration of y = 25 mol% ($U_{1-y}Nd_yO_{2-x}$) could be reached.

Keywords: uranium oxide microspheres, sol-gel, starch, porosity, infiltration, neodymium, americium.

* Corresponding author
E-mail address: gamze.colak@sckcen.be (G. Çolak)
Phone: +32 14 33 82 38

1. Introduction

Nuclear energy is commonly employed to generate large amounts of electricity on demand, at a very low carbon footprint. However, one of the challenges in the utilization of nuclear energy is the management of spent nuclear fuel, which presents a long-term radiological hazard. The issue is relevant to sustain the further deployment of nuclear power as a low-carbon energy source, as well as to deal with the accumulated spent fuel in a phase-out scenario. The long-term radiotoxicity and heat load of spent fuel after uranium and plutonium recycling is primarily caused by a group of elements known as the minor actinides (MAs). In particular, americium dominates the heat emission and radiotoxicity of MAs for several thousands of years, although it represents less than 0.1 wt.% in spent UO_2-based fuel from light water reactors [1]. A possible solution to reduce the radiological impact is to partition the spent fuel in separate waste fractions such as uranium, plutonium, the MAs, and fission products, which are further managed individually (partitioning and conditioning). This could eventually be followed by the transmutation of minor actinides into lighter, short-lived isotopes in thermal- and fast-neutron spectrum reactors [2].

Several research programs have been dedicated to investigating the transmutation of MA-containing transmutation targets by looking at different fabrication routes, the in-reactor behavior and post-irradiation examinations [3-6]. Particular effort is put on the development of fabrication routes to address various needs such as the type of host matrix and content of the MA element, the physico-chemical properties of the target material, and reduced radiological hazards during handling [7]. In support of these studies, so-called simulated transmutation targets are also being used, where the radiotoxic MA element is replaced by an inactive representative surrogate element [8]. Certain lanthanides are commonly used as surrogates for actinides owing to their similar chemical behavior and closely matching ionic radii [9]. For example, trivalent neodymium (Nd) in an eight-fold coordination (r = 1.11 Å) is an excellent surrogate for trivalent americium (Am) with the same coordination number (r = 1.09 Å).

Transmutation targets may be manufactured in a way similar to that of commercial uranium and mixed uranium-plutonium oxide fuels, *via* powder metallurgical processes [8,10-13]. However, a major drawback lies in the generation of dust containing radioactive MA isotopes, which will accumulate in filters and on the walls of shielded infrastructure, posing a radiological hazard [14]. A possible remediation is the use of aqueous conversion routes to produce microspheres, which can be directly used as sphere-pac or vipac fuel [15], or alternatively, be manufactured into pellets [16]. One important disadvantage of these routes is the generation of liquid waste streams loaded with MA traces, which are often complicated and expensive to dispose.

One particular innovation in response to all the aforementioned issues has been the application of infiltration (or impregnation) of host matrix materials such as yttria-stabilized zirconia (YSZ) or uranium dioxide with concentrated aqueous solutions containing MAs [5]. The use of infiltration meets three important criteria: (a) It avoids formation of powdered dust when combined with an aqueous conversion route to produce the host matrix; (b) The generation of MA-containing liquid waste is essentially avoided; and (c) It minimizes the

steps requiring a shielded environment, improving efficiency and safety [8]. The infiltration procedure may be repeated several times in order to reach the saturation limit of the matrix material [17]. The MA loaded target materials are subsequently dried, calcined and sintered to obtain the desired chemical composition and physical properties.

The infiltration process requires the fabrication of a porous host matrix material, such as low density pellets *via* conventional powder processing or microspheres prepared by sol-gel routes like external or internal gelation. In most of the related studies [8,18-22], the external gelation process has been applied to fabricate inert matrices (YSZ or MgO) or uranium oxide-based matrices for infiltration. An early comparative study by Somers and Fernandez of infiltration efficiency with internal and external gelation produced YSZ showed a better infiltration performance with external gelation, which was attributed to the decomposition of the organic polymer (Polyvinyl alcohol) used in the external gelation route [23]. A later study by Couland *et al*. confirmed that for high infiltration efficiencies, YZS produced by internal gelation needed the addition of pore-former, and that higher dopant levels can be achieved by repeating the infiltration and calcination steps several times [17]. The permeability of kernels fabricated *via* both sol-gel processes was also extensively studied in the field of biopolymers for drug encapsulation, where both types were reported with potential use [24].

Even though internal gelation was less explored in previous infiltration studies for uranium-based nuclear fuels, it was not *a priori* rejected. Within the SPHERE irradiation experiment a mixed-oxide particle fuel (composition $U_{0.76}Pu_{0.20}Am_{0.03}O_{2-x}$) was developed by infiltration of porous beads prepared from external and internal gelation with americium solution [25]. In the later MARINE irradiation experiment the fabrication of mixed-oxide fuels with Am contents up to 14 % metal fraction similarly employed infiltration, but the precursors were made using external gelation only [26]. Recently, the application of infiltration on internally gelled UO_3 microspheres was also reported for manganese and chromium doping (up to 2000 ppm, dopant to uranium weight concentration) [27]. In general, infiltration on internally gelled support matrices has been applied successfully for low dopant levels (up to 3 mol%) by several research groups, but its application on internally gelled uranium oxide microspheres for high dopant concentrations has not yet been reported.

In this work, we studied the effect of calcination temperature and the use of pore-formers on the microstructure of uranium oxide-based microspheres, prepared *via* internal gelation. The objective was to tailor density, porosity and specific surface area, to determine the conditions to obtain microspheres that are well-suited for infiltration purposes. Microspheres from the most promising routes were subsequently used for infiltration with neodymium solution (targeted y = 0, 5, 10, 20, 30 mol% in $U_{1-y}Nd_yO_{2-x}$) and analyzed by X-ray diffraction after sintering.

2. Experimental

2.1. Chemicals

Uranium dioxide powder (UO_{2+x}), depleted in $^{235}_{92}U$ (0.3 wt.% ^{235}U) and of nuclear-grade purity was obtained from AREVA. Nitric acid aqueous solution ($w(HNO_3)$ =70 wt.%, purity > 99.9 wt.%), ammonia aqueous solution ($w(NH_3)$ =30 wt.%, purity > 99.5 wt.%), urea (purity > 99.5 wt.%), Hexamethylenetetramine (HMTA) (purity ≥ 99.0 wt.%), graphite (<20 µm grain size, purity > 99.0 wt.%**)** and starch (< 20 µm grain size, purity > 99.0 wt.%) were purchased from Sigma-Aldrich®. Silicone oil (Polydimethylsiloxane, kinematic viscosity 1 cm^2/s at room temperature) and petroleum benzine (313 K to 333 K boiling range, purity > 99.9 wt.%) were purchased from VWR™. The trivalent lanthanide precursor, $Nd(NO_3)_3{\cdot}6H_2O$ was purchased from Strem Chemicals Inc™ (purity ≥ 99.9 wt.%).

2.2. Synthesis of microspheres by internal gelation (IG)

Ammonium diuranate (ADU), $3UO_3{\cdot}2NH_3{\cdot}4H_2O$, microspheres were prepared *via* IG using an Acid-Deficient Uranyl Nitrate (ADUN) solution as uranium precursor. The preparation of the ADUN solution (c(U)= 2.6 mol/L, $\frac{c(NO_3^-)}{c(U)}$ = 1.56) has been described by Schreinemachers *et al*. [28]. An aqueous solution containing the gelation agents urea and HMTA in equal concentration (3.1 mol/L) was prepared and cooled in an ice bath to around 273 K. The sol was prepared by mixing the gelation agent solution with pre-cooled ADUN solution in a 1:1 (vol.%) ratio, leading to c(U) = 1.3 mol/L. The amount of gelation agents in the sol is defined by their molar amount over the molar metal amount (R value). With an uranium concentration of 1.3 mol/L in the sol, the R value was 1.2 for both gelation agents. In experiments where the effect of pore-formers was investigated, solid starch or graphite was additionally added to the sol (60 g/L). The cooled sol was subsequently inserted in a syringe with a hollow needle and immediately inserted as droplets into a double-walled glass column filled with silicon oil at 363 K, allowing to convert the aqueous droplet feed into gelled microspheres. The heat transfer into the droplets initiates the conversion from liquid to gelled microspheres [29]. After gelation, the microspheres were collected *via* a sieve, washed 3 times with 50 mL of petroleum benzine, and aged in 100 mL NH_3 (aq.) (12.5 wt.%) for 24 h. After ageing, the microspheres were washed twice with 50 mL of the same NH_3 (aq.) solution and dried in a vacuum furnace at 50 mbar and 363 K for 24 h.

2.3. Thermal treatments and infiltration of microspheres

The process followed for performing the infiltration of uranium oxide microspheres is presented schematically in Figure 1. Firstly, the dried ADU microspheres were loaded in alumina crucibles and subjected to a calcination treatment at a predetermined temperature T_{cal} for 2 h (specific calcination temperatures are given in Table 1), using a Nabertherm LT 9113/P330 muffle furnace operating in ambient air atmosphere. Subsequently, a known amount of calcined microspheres were subdivided in four separate quartz crucibles. A stock solution of neodymium nitrate (c(Nd) = 2.4 mol/L) was prepared by dissolving $Nd(NO_3)_3{\cdot}6H_2O$ in ultra-pure water, and two aliquots were further diluted to 0.4 and 0.8 mol/L to reach the aimed dopant concentrations. The volume of infiltrant solution was

approximately 250 µL for all sub-batches. A calculated volume of the aliquots was added to the quartz crucibles to reach a targeted Nd metal fraction, $\chi(\mathrm{Nd}) = \frac{n(\mathrm{Nd})}{n(\mathrm{U+Nd})}$, of 5 or 10 mol%, respectively. The solution was left to infiltrate into the uranium oxide microspheres overnight and it was observed that the microspheres absorbed all the liquid. To reach a targeted χ(Nd) of 20 mol%, a sub-batch infiltrated up to χ(Nd) = 10 mol% was first re-calcined at the original calcination temperature (see Table 1), and subsequently re-infiltrated with the 0.8 mol/L neodymium nitrate aliquot to reach χ(Nd) = 20 mol%. The targeted χ(Nd) of 30 mol% was reached in 3 consecutive infiltration steps with intermediate calcination. A final calcination treatment at 1173 K for 2 h was performed on all infiltrated microspheres.

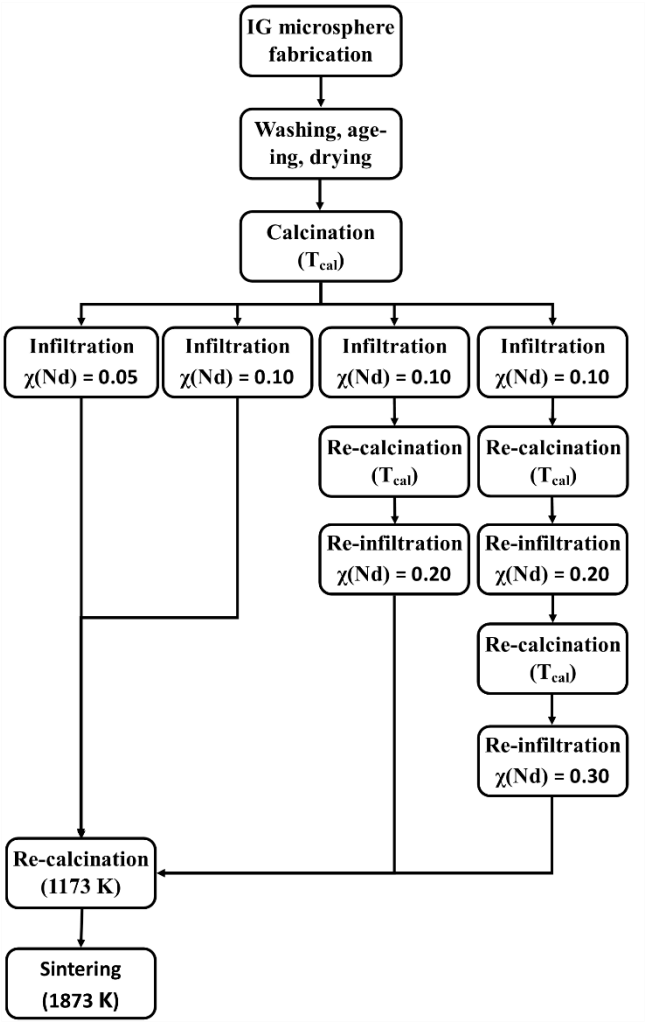

Figure 1. Schematic showing the process steps to perform infiltration and obtain sintered $U_{1-y}Nd_yO_{2-x}$ microspheres (y = 5, 10, 20, and 30 mol%).

The calcined microspheres were loaded in molybdenum crucibles and sintered under reducing conditions (Linn High Therm, HT-1800-Moly). The thermal profile consisted of a first heating stage in Ar atmosphere up to 973 K (5 K/min), at which point the gas atmosphere was changed to an Ar/H_2 (96:4) - Ar/O_2 (99.5:0.5) gas mixture with flow rates of 1429 mL/min and 71 mL/min, respectively, to obtain an oxygen potential of -420 kJ/mol at 1873 K. The

isotherm time was 2 h at 973 K before the temperature was increased to 1873 K (5 K/min). A dwell time of 10 h was maintained at the sintering temperature, after which the atmosphere was switched back to Ar (1500 mL/min). Finally, the sintered microspheres were cooled to 298 K at a rate of 5 K/min.

2.4. Thermogravimetric analysis (TGA)

TGA analysis was performed using a Setaram Setsys Evolution 16/18 coupled to a Pfeiffer Omnistar GSD320 mass spectrometer (MS) analyzer. TGA measurements were carried out in Al_2O_3 crucibles, using a Type S thermocouple rod. A heating rate of 10 K/min and a sample mass of about 30 mg was applied. The set-up was first evacuated to $\leq$ 0.15 mbar and purged 3 times with Ar before introducing synthetic air (60 mL/min) into the furnace. The temperature program contained isothermal segments at 308 K at the beginning (30 min) and the end (60 min) of each analysis. The tare mass of the crucible, as well as the mass of the crucible containing the sample was measured prior to and after each TGA analysis (Mettler-Toledo AT201), with an uncertainty of ± 0.03 mg (2σ).

2.5. X-ray diffraction analysis

Crystallographic studies on calcined and sintered microspheres were conducted at room temperature by powder X-ray diffraction (Bruker© D8 Advance diffractometer), operating in Bragg-Brentano configuration and using a Cu-LFF X-ray tube (Cu $K_{\alpha 1}$ = 0.15405929 nm [30]) at 40 mA and 40 kV. Diffracted X-rays were detected by a position-sensitive real time multiple strip detector (Lynxeye) operated in continuous position-sensitive detection (PSD) mode, with a PSD opening of 3.3° (2θ). The incident beam was collimated by a variable divergence slit set to an illumination length of 15 mm, and axial Soller slits of 2.5°. The diffracted beam passed through axial Soller slits of 2.5° and a Ni filter. Both types of microspheres (calcined and sintered) were ground in a ceramic mortar and a small amount of the resulting powder was dispersed on top of a zero-background silicon single crystal holder. After sample preparation, the specimen was mounted onto a rotating sample stage and diffractograms were recorded while applying a rotation speed of 15 rotations/min. Diffractogram acquisitions were performed by scanning from 15° - 90° with a step size of 0.03 °(2θ) for calcined microspheres, and from 20° - 120° (2θ) with a step size of 0.015 °(2θ) for sintered microspheres. The goniometer alignment was calibrated using a sintered alumina disc (NIST Standard Reference Material 1976b) and validated at regular intervals using the same reference material. The X-ray diffractograms were evaluated with HighScore Plus software (v4.9), employing unit cell refinement based on the Nelson-Riley method for calculating lattice parameters.

2.6. Microscopy

Optical Microscopy (OM) observations of the calcined microspheres were performed with a Hirox© MX-2016Z microscope. Before each analysis, images of a calibration standard were recorded (Keyence OP-88141). A Hi-Scope Advanced KH-3000 system (Hirox©) was used for data acquisition. Microspheres with different calcination temperature of each composition were analyzed. Scanning Electron Microscopy (SEM) was conducted on calcined microspheres using a JEOL JSM 7100-FA™ field-emission scanning electron microscope

located in a hot cell, equipped with a secondary and backscattered electron detector. The working distance ranged from 9 mm to 11 mm and an accelerating voltage of 5 kV was employed.

2.7. Specific surface area analysis and density measurements

The specific surface area of calcined microspheres were determined according to the Brunauer-Emmett-Teller (BET) method [31] using a Micromeritics Tristar® II 3020 surface and pore analyzer. Samples were degassed in vacuum environment and heated at 523 K for 2 h prior to the start of the measurement. The specific surface area was obtained by determination of the 77 K adsorption isotherm of nitrogen gas. A Dewar filled with liquid nitrogen was used to cool the samples during the measurement.

True density values of sintered and calcined microspheres were obtained using a gas displacement pycnometry system AccuPyc™ II 1340. The gas pycnometer uses helium as displacement gas and is controlled *via* the software AccuPyc™ II 1340 V1.5 (Micromeritics Instrument Corporation). The set-up (1 mL cell volume) has been calibrated using a standard with a certified volume of 718.51 ± 0.05 µL. After the calibration, a verification measurement took place by measuring the calibration standard as unknown sample. Verification step is repeated after each measurement. The total closed porosity (*i.e.* impermeable to He molecules) is derived from the ratio of true density ($\rho_{\text{pycnometry}}$) to theoretical density ($\rho_{\text{theoretical}}$).

Liquid intrusion porosimetry was used as additional technique for density measurements, combined with calculations of accessible and inaccessible porosity [32]. Distilled water and a few drops of surfactant were used as intrusion liquid (ρ_{liquid}=0.998 g/cm^3). Microspheres (~ 200 mg) were placed inside a Pt crucible and weighed on a precision scale (Mettler-Toledo© AT201). Subsequently, the Pt crucible was fully immersed in the intrusion liquid and weighed again (Sartorius® balance ED124S combined with immersion kit YDK01LP). Afterwards, the Pt crucible is removed from the liquid and microspheres were transferred onto a paper tissue to remove superficial liquid from the surfaces. Finally, one last weight measurement was performed on the precision scale (Mettler-Toledo© AT201). The apparent density and accessible porosity are derived from the measurements and the theoretical density according to equations (1) to (6) outlined below. The method probes the open porosity accessible to intrusion with an aqueous solution, resembling conditions used during infiltration.

From the theoretical density ($\boldsymbol{\rho_{\text{theoretical}}}$) and the mass of the sample prior to immersion in the penetrating liquid ($\boldsymbol{m_{\text{dry}}}$), the theoretical volume ($\boldsymbol{V_{\text{theoretical}}}$) is readily obtained:

$$\boldsymbol{V_{\text{theoretical}}} = \frac{\boldsymbol{m_{\text{dry}}}}{\boldsymbol{\rho_{\text{theoretical}}}} \quad (1)$$

The porosity volume, inaccessible for impregnation ($\boldsymbol{V_{\text{inaccessible}}}$), and consisting of the truly closed pores and the porosity which is either too fine or which is otherwise inaccessible, is derived from the apparent mass of the sample when weighed submerged in the penetrating liquid ($\boldsymbol{m_{\text{wet,in}}}$), the true mass of the sample ($\boldsymbol{m_{\text{dry}}}$), and the density of the liquid ($\boldsymbol{\rho_{\text{liquid}}}$):

$$\boldsymbol{V_{\text{inaccessible}}} = \frac{\boldsymbol{m_{\text{dry}}} - \boldsymbol{m_{\text{wet,in}}}}{\boldsymbol{\rho_{\text{liquid}}}} - \boldsymbol{V_{\text{theoretical}}} \quad (2)$$

The porosity volume, accessible for impregnation ($\boldsymbol{V_{accessible}}$), is derived from the difference of the true mass of the sample ($\boldsymbol{m_{dry}}$), and the mass of the sample after removing it from the penetrating liquid and wiping off the surface, but otherwise leaving the liquid inside the accessible pores ($\boldsymbol{m_{wet,out}}$):

$$\boldsymbol{V_{accessible}} = \frac{\boldsymbol{m_{wet,out}} - \boldsymbol{m_{dry}}}{\boldsymbol{\rho_{liquid}}} \quad (3)$$

The fraction of accessible and inaccessible porosity is subsequently defined as:

$$\textbf{accessible porosity}\ (\%) = \frac{\boldsymbol{V_{accessible}}}{\boldsymbol{V_{accessible}} + \boldsymbol{V_{inaccessible}}}\ \% \quad (4)$$

$$\textbf{inaccessible porosity}\ (\%) = \frac{\boldsymbol{V_{inaccessible}}}{\boldsymbol{V_{accessible}} + \boldsymbol{V_{inaccessible}}}\ \% \quad (5)$$

The apparent density ($\boldsymbol{\rho_{apparent}}$) is the ratio of the true mass of the sample to its apparent volume:

$$\boldsymbol{\rho_{apparent}} = \frac{\boldsymbol{m_{dry}}}{\boldsymbol{V_{apparent}}} = \frac{\boldsymbol{m_{dry}}}{\boldsymbol{V_{theoretical}} + \boldsymbol{V_{accessible}} + \boldsymbol{V_{inaccessible}}} \quad (6)$$

3. Results

3.1. Effect of calcination temperature and the use of pore-formers

An efficient infiltration process requires that the microspheres, as the infiltration medium, are porous and do not readily dissolve/disintegrate in the dopant nitrate solution. The first approach applied in this study to tailor the microstructure, has been to decrease the calcination temperature from the conventional 1173 K to 1073 K, 923 K, 823 K and 773 K on microspheres without pore-former. The effect of the calcination temperature on microsphere microstructural parameters such as Specific Surface Area (SSA), density and porosity is summarized in Table 1.

Table 1. Overview of the type of crystalline compound with associated theoretical density, and microstructural characteristics (SSA, apparent density, true density and porosity levels) in microspheres without pore-formers after calcination at the designated temperatures. Apparent and true densities are expressed relative to the theoretical density, in % TD units.

T_{cal} (K)	773	823	923	1073	1173
Compound	UO_3	$UO_3 + U_3O_8$	U_3O_8	U_3O_8	U_3O_8
Theoretical density (g/cm^3)	6.800	7.002[a]	8.246	8.246	8.246
SSA (m²/g)	14.1 ± 0.1	24.7 ± 0.1	10.8 ± 0.1	6.0 ± 0.1	2.3 ± 0.1
True density (% TD)	85 ± 1	88 ± 1	97 ± 1	98 ± 1	97 ± 1
Closed porosity (%)	15 ± 1	12 ± 1	3 ± 1	2 ± 1	3 ± 1
Apparent density (% TD)	59 ± 1	65 ± 4	75 ± 1	89 ± 2	94 ± 1
Accessible porosity (%)	23 ±1	18 ± 5	13 ± 1	5 ± 2	3 ± 1
Inaccessible porosity (%)	18 ± 1	17 ± 5	12 ± 1	5 ± 2	3 ± 1

[a] Based on a 86 wt.% β-UO_3 and 14 wt.% α-U_3O_8 composition as found by XRD phase quantification *via* Rietveld refinement

The calcination treatment and chosen temperature determines to which uranium oxide phase the dried ADU microspheres are converted (see also Figure 2). β-UO_3 was formed at a calcination at 773 K, whereas α-U_3O_8 was obtained at and above 923 K. Microspheres calcined at 823 K presented a mixture of β-UO_3 and α-U_3O_8 in a 86:14 weight ratio, as determined from Rietveld analysis of the XRD pattern. The SSA values show a maximum (24.7 m²/g) for the 823 K calcined microspheres, and a decreasing trend occurs with more elevated calcination temperature. The density clearly increases with calcination temperature, and conversely, the porosity decreases. The lowest calcination temperatures (773 and 823 K) result in very porous structures with an apparent density around 60% TD and a significant level of accessible porosity (around 20%). The higher calcination temperatures (823 to 1173 K) result in microspheres with little remaining porosity. Note that the difference in

closed/inaccessible porosity measured by gas pycnometry and water intrusion is related to the medium. The liquid intrusion provides values of porosity accessible by water. On the other hand, gas pycnometry provides porosity linked to the accessibility of He gas molecules which are inert and much smaller than water molecules. Lower calcination temperatures are the most appropriate for infiltration purposes.

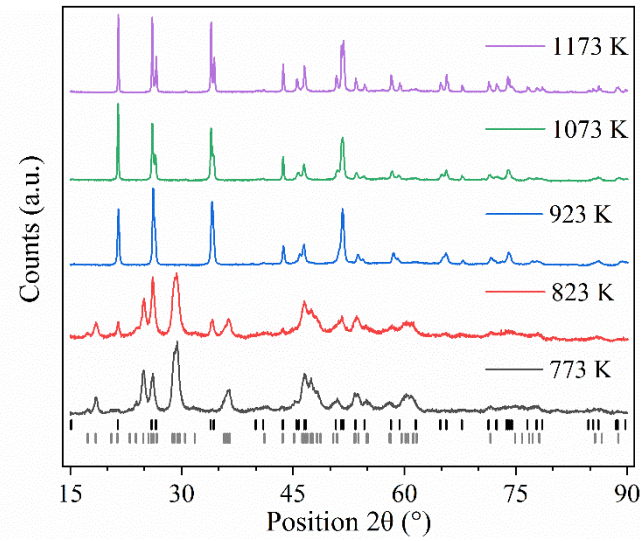

Figure 2. Room temperature XRD patterns of internally gelled microspheres, after calcination at different temperatures (indicated in the legend). At the bottom of the figure vertical lines indicate peak positions of the α-U_3O_8 (black) and β-UO_3 (grey) phases. To improve readability only reflections with a relative intensity above 4% are shown.

A second approach to tailor the microstructure of the microspheres involved the addition of starch or graphite as pore-formers to the initial sol used in the internal gelation process. The addition of pore-formers contributes to the final microstructure by their decomposition into volatile compounds (mainly CO_2) during the calcination step. Therefore, the decomposition behavior of the pore-formers during calcination was first evaluated using TGA (Figure 3). The results show that starch requires approximately 793 K to completely decompose, in agreement with reports by Mann *et al*. [33]. In contrast, graphite requires a much higher temperature (approximately 1073 K) to decompose completely, as was also demonstrated in the work of Nästrén *et al*. [21]. Therefore, calcination temperatures between 823 K and 1073 K in air were considered for the microspheres containing pore-formers.

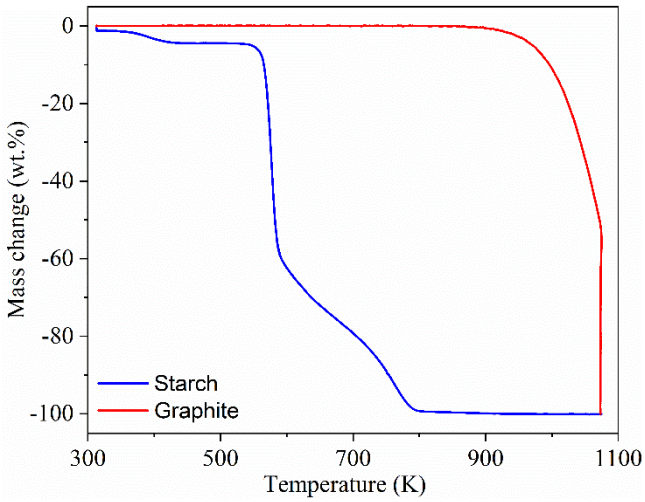

Figure 3. TGA showing the mass change of starch and graphite during calcination up to 1073 K. The decomposition of starch starts at 533 K and is completed at 793 K, whereas temperatures up to 1073 K are required for the oxidation of graphite.

Table 2. Overview of the type of crystalline compound with associated theoretical density, and microstructural characteristics (SSA, apparent density, true density and porosity levels) in pore-former doped microspheres after calcination at the designated temperatures. Apparent and true densities are expressed relative to the theoretical density ($\rho_{theoretical}$), in % TD units.

Pore-former	**Starch**			**Graphite**		
T_{cal}	**823 K**	**923 K**	**1073 K**	**823 K**[b]	**923 K**[b]	**1073 K**
Compound	UO_3	U_3O_8	U_3O_8	UO_3 + U_3O_8	U_3O_8	U_3O_8
$\rho_{theoretical}$ **(g/cm^3)**	6.800	8.246	8.246	6.916[a]	8.246	8.246
SSA (m²/g)	18.9 ± 0.1	5.8 ± 0.1	4.1 ± 0.1	13.3 ± 0.1	5.7 ± 0.1	2.4 ± 0.1
True density (% TD)	96 ± 1	99 ± 1	99 ± 1	98 ± 1	98 ± 1	99 ± 1
Closed porosity (%)	4 ± 1	1 ± 1	1 ± 1	2 ± 1	2 ± 1	1 ± 1
Apparent density (% TD)	64 ± 2	53 ± 1	96 ± 1	77 ± 6	61 ± 1	84 ± 1
Accessible porosity (%)	34 ± 5	33 ± 1	2 ± 1	18 ± 9	25 ± 1	4 ± 1
Inaccessible porosity (%)	3 ± 5	14 ± 1	2 ±1	5 ± 9	14 ± 1	12 ± 1

[a] Based on a 92 wt.% β-UO_3 and 8 wt.% α-U_3O_8 composition as found by XRD phase quantification *via* Rietveld refinement.
[b] Samples contain remaining graphite impurities

The combined effect of calcination temperature and the use of pore-formers on the microstructural parameters such as specific surface area (SSA), density and porosity is summarized in Table 2. Similarly to Table 1, the difference in closed/inaccessible porosity measured by gas pycnometry and water intrusion is related to the medium. The type of uranium oxide phase obtained after calcination was determined by XRD analysis (see Figure 4), and similar results as function of calcination temperature were observed, except that the starch-doped microspheres calcined at 823 K consisted of β-UO_3 without any traces of α-U_3O_8. This shows that after calcination at 823 K, the phase composition of the microspheres with either starch or graphite pore-formers are different. After calcination at 823 K and 923 K, both the SSA and the accessible porosity is higher for the starch-doped microspheres. This is linked to the fact that all samples prepared with the graphite pore-former and calcined at temperatures below 1073 K contained significant amounts of residual graphite, owing to the incomplete decomposition, which affects the density and porosity values.

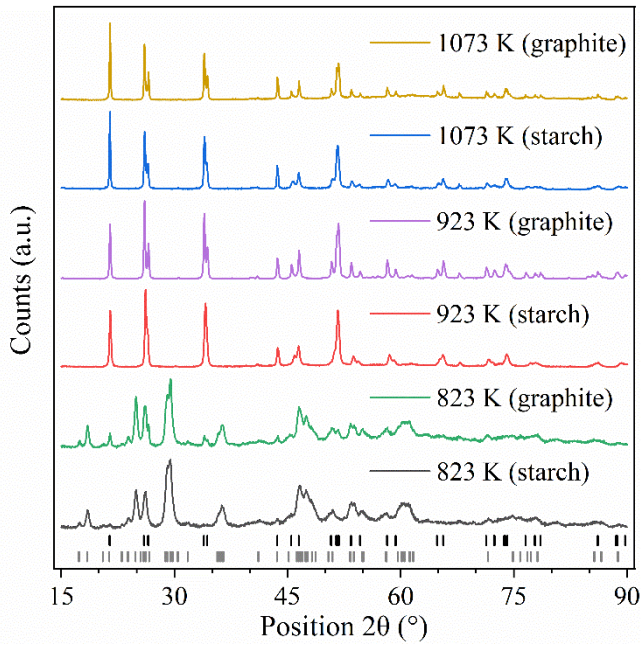

Figure 4. Room temperature XRD patterns of internally gelled microspheres with pore-formers, after calcination at different temperatures (indicated in the legend). At the bottom of the figure vertical lines indicate peak positions of the α-U_3O_8 (black) and β-UO_3 (grey) phases. To improve readability, only reflections with a relative intensity above 4% are shown. The ceramics are composed of α-U_3O_8 after calcination at 923 K or 1073 K. After calcination at 823 K either a mixture of β-UO_3 and α-U_3O_8 (graphite pore-former) or pure β-UO_3 (starch pore-former) was obtained.

All ceramics prepared with starch were found to be phase-pure after calcination, and no remaining organic impurities from the pore-former are expected based on the TGA analysis. The SSA was at a maximum in 823 K calcined microspheres, and decreased with increasing calcination temperature. A minimum in apparent density was observed after calcination at 923

K, but comparable levels of accessible porosity were measured after calcination at 823 K. Calcination at 1073 K seems to result in the least favorable parameters, *i.e.* high density and little porosity.

Samples prepared with graphite as pore-former similarly had the lowest apparent density after calcination at 923 K, and the porosity levels in general were significantly lower as compared to their starch-doped counterparts. Based on the TGA results, a temperature above 1073 K is required to fully decompose the graphite, but at such elevated calcination temperatures, the accessible porosity decreases to unfavorably low values for subsequent impregnation. Therefore, the use of graphite as pore-former in combination with the effects of calcination temperature seem of little added value towards tailoring the microstructure of uranium oxide microspheres for infiltration.

In conclusion, microspheres without pore-formers and calcined at low temperature (773 or 823 K) and microspheres with addition of starch and calcined at 823 K show the most promising microstructural parameters towards infiltration. To provide additional experimental evidence, optical and scanning electron microscopy were performed on the aforementioned set of microspheres (see Figure 5). The microstructure of all three samples is quite different. After calcination at 773 K the UO_3 microsphere surface appears very smooth, in contrast to the very rough and porous surface of the biphasic (UO_3 + U_3O_8) microsphere calcined at 823 K. The starch doped UO_3 microsphere calcined at 823 K also has a rather smooth surface, but large macropores (pore widths exceeding 50 nm [34]) can be clearly distinguished. The biphasic microspheres obtained after calcination at 823 K and without the use of a pore-former were notably more brittle during handling (e.g. deformation after manipulation with tweezers), compared to both other series which produced phase-pure UO_3 microspheres.

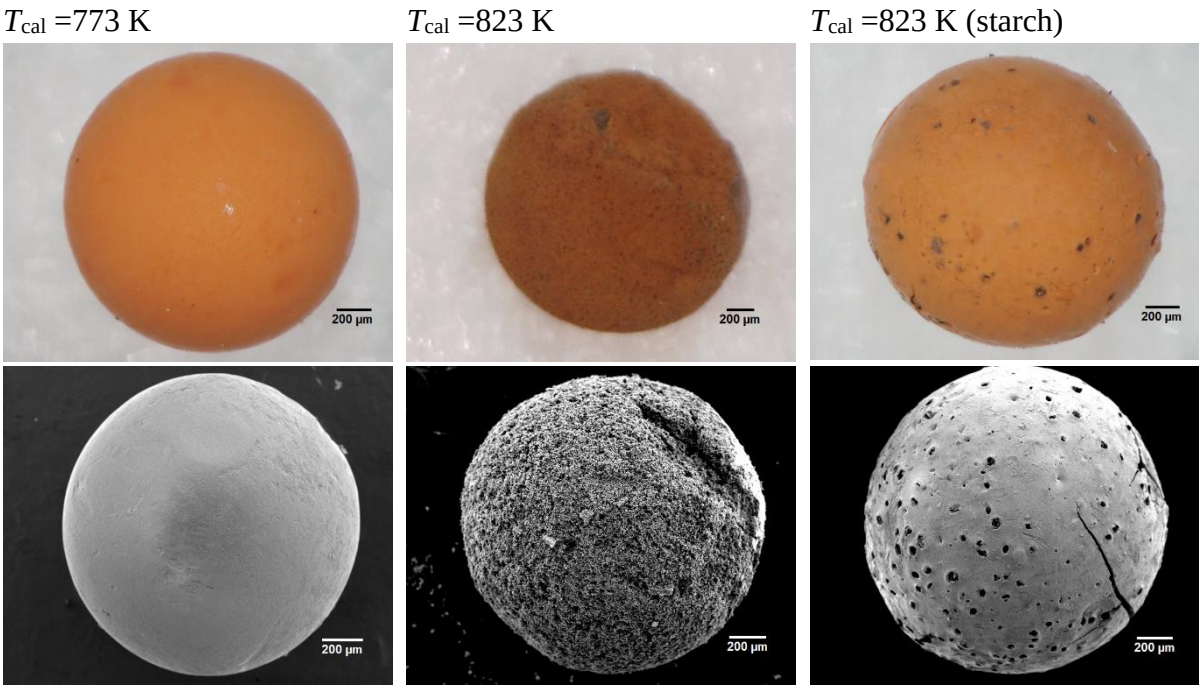

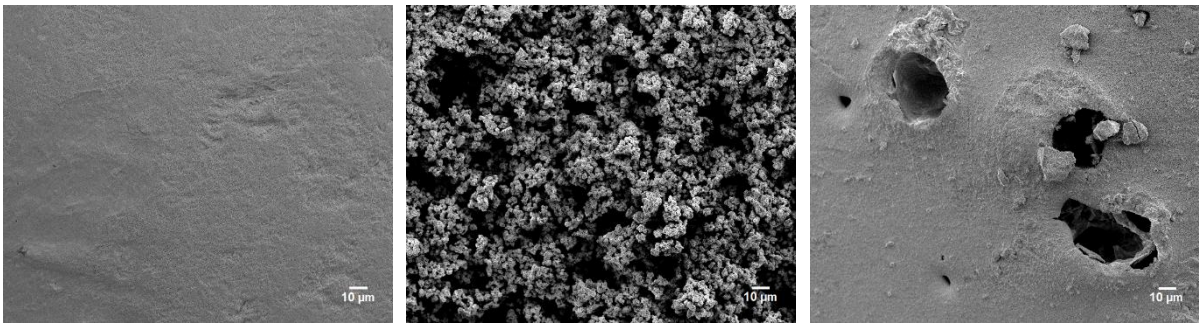

Figure 5. OM (top row) and SEM micrographs (bottom two rows) of microspheres without pore-formers calcined at 773 K and 823 K, and with addition of starch pore-former calcined at 823 K. Note that the gelled microspheres have slightly varying diameters. The size might change with calcination temperature and addition of pore-formers.

3.2.Infiltration tests

According to the results obtained from the microstructure tailoring (see section 3.1) the microspheres without pore-formers calcined at 773 K and 823 K, and microspheres doped with starch and calcined at 823 K were selected for infiltration tests. In all three cases the experimental procedure outlined in section 2.2.3 (see Figure 1) was applied to infiltrate, calcine and sinter $U_{1-y}Nd_yO_{2-x}$ microspheres with a targeted Nd content of y = 5, 10, 20, and 30 mol%. Densities of the sintered microspheres were measured by gas pycnometry and ranged between 82−90% TD. XRD was used to investigate the quality of the products after sintering, *i.e.* formation of a single solid solution between dopant and uranium oxide matrix, and to quantify the difference between targeted and actual Nd content by evaluating the lattice parameter.

Figure 6 shows the high 2θ region of the XRD patterns from all three sets of $U_{1-y}Nd_yO_{2-x}$ microspheres. Diffractograms covering the entire angular range are available in the ESI. The expected peak shift to a higher 2θ angle with increased Nd-dopant content is clearly visible in the patterns of microspheres calcined originally at 823 K. In these patterns, no shoulder peaks or peak splitting is observed, pointing to the formation of a single solid solution between Nd dopant and uranium oxide matrix. However, some increased peak broadening is apparent in the ceramics with the highest dopant content, which may indicate some variation in the actual Nd concentration. Furthermore, for targeted Nd concentrations of 20 and 30 mol% there appears to be a significant discrepancy between the peak positions of the sintered microspheres prepared from the 773 K calcined precursors without pore-former, and the two other sets. This indicates that the extent of infiltration was not the same, *i.e.* different amounts of Nd were incorporated. On the other hand, the diffraction patterns of the sintered microspheres calcined at 823 K with and without starch addition closely agree with each other.

To quantify the observations made in Figure 6, the lattice parameters of the $U_{1-y}Nd_yO_{2-x}$ phases were measured, and compared against values reported in literature. Several studies have been performed throughout the years [35-40], of which some display a discrepancy from the ideal Vegard's law behaviour, *i.e.* a single linear dependency between Nd content and lattice parameter does not exist over the full range of Nd concentrations. Recently however, it was found that this dependency needs to be described by two distinct relations, because of competing charge compensation mechanisms [35,41]:

$$a(y) = \mathrm{a}_0 - 6.57(13) \times 10^{-4} \cdot y \quad [\text{Å}] \quad (y \leq 0.10) \tag{7}$$

$$a(y) = \mathrm{a}_0 - 5.24(13) \times 10^{-4} \cdot y \quad [\text{Å}] \quad (0.15 \leq y \leq 0.30) \tag{8}$$

with $a(y)$ the cubic lattice parameter of the $U_{1-y}Nd_yO_{2-x}$ phase as function of Nd content (y), and a_0 the lattice parameter of UO_2 (5.47127(8) Å [42]). In this work identical sintering conditions were applied as in the work of Schreinemachers *et al*. [35], which allowed to evaluate the measured lattice parameters and to derive the corresponding "actual" Nd concentration y in the infiltrated microspheres after sintering from equations (7) and (8), see Figure 7 and Table 3.

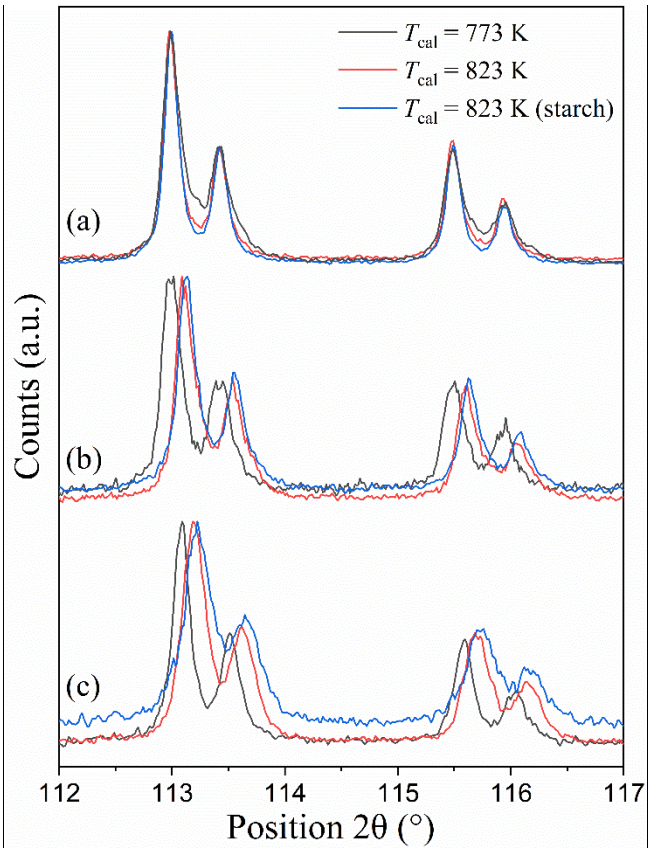

Figure 6. Room temperature XRD patterns (high-angle reflections shown only) of sintered $U_{1-y}Nd_yO_{2-x}$ microspheres, prepared by infiltration with a targeted Nd concentration of y = 10 mol% (a), y = 20 mol% (b) y = 30 mol% (c). The calcination temperature (T_{cal}) applied prior to the infiltration is displayed in the legend to distinguish between the samples. Note that each reflection consist of the Cu $K\alpha_{1,2}$ doublet. Each individual pattern was corrected for sample displacement and normalized to the maximum intensity of the 113 ° (2θ) reflection.

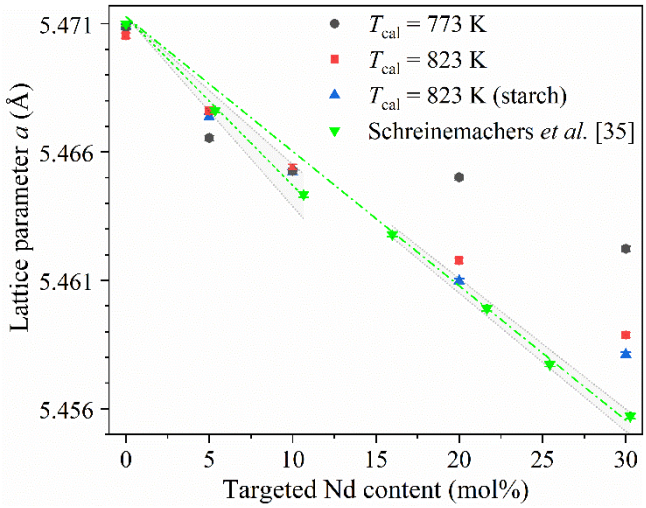

Figure 7. Lattice parameters as a function of the targeted Nd content in infiltrated and sintered microspheres. Uncertainties are given at a 95% confidence level (±2σ). Results reported by

Schreinemachers *et al*. on internally gelled and sintered $U_{1-y}Nd_yO_{2-x}$ microspheres are used as reference, here showing also the linear fit with 95% confidence interval in both low (< 15 mol%) and higher (>15 mol%) concentration ranges [35].

Table 3. Overview of measured lattice parameters and comparison between targeted and actual dopant concentration (Nd mol%) in the infiltrated microspheres after sintering.

T_{cal} (K)	Pore-former	Target χ(Nd) (mol%)	Lattice parameter *a* (Å)	Actual χ(Nd) (mol%)
773	none	0	5.4709(1)	-
		5	5.4663(1)	7.2(4)
		10	5.4653(1)	9.1(4)
		20	5.4651(1)	9.5(4)
		30	5.4623(1)	17.3(4)
823	none	0	5.4705(1)	-
		5	5.4676(1)	5.6(4)
		10	5.4654(1)	8.9(4)
		20	5.4618(1)	18.1(4)
		30	5.4589(1)	23.7(4)
823	starch	0	5.4709(1)	-
		5	5.4674(1)	5.9(4)
		10	5.4652(1)	9.2(4)
		20	5.4610(1)	19.7(4)
		30	5.4581(1)	25.1(4)

The measured lattice parameters and a comparison between the targeted and actual Nd content in each of the samples is summarized in Table 3. For the dopant target concentrations of 5 mol% and 10 mol%, all infiltrations were successful. Only in the 773 K series the actual concentration (7.2 mol%) deviated slightly from the target concentration of 5 mol% whereas the other samples were closer to the targeted 5 mol%. For higher dopant concentrations (20 mol% and 30 mol%) not all infiltrations were successful. The maximum dopant concentration for the microspheres calcined at 773 K was limited to 17 mol%, whereas approximately 25 mol% dopant concentration was achieved with microspheres calcined at 823 K with and without starch pore-former.

In the infiltration process (see Figure 1) applied here successive re-calcination and re-infiltration steps were performed on the microspheres to reach Nd contents higher than 10 mol%. A possible simplification would be to adapt the dopant nitrate solution concentration to target immediately the higher concentrations, as presented schematically in Figure 8, where the host matrix is infiltrated in a single step. The simplified infiltration process was tried out on a batch of microspheres prepared without pore-formers and calcined at 823 K. The infiltrated microspheres were sintered under identical conditions as the previous samples, and subjected to XRD for lattice parameter evaluation. A summary of the results is presented in Table 4, and the XRD patterns are available in the ESI. However, the efficiency of infiltration seemed to be less good, as significant differences between targeted and actual Nd concentration were observed.

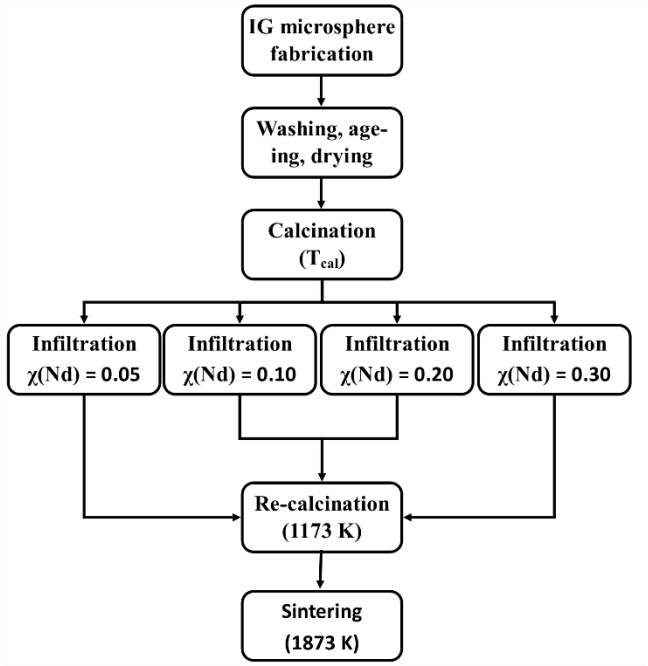

Figure 8. Schematic showing the simplified process steps to perform infiltration and obtain sintered $U_{1-y}Nd_yO_{2-x}$ microspheres (y = 5, 10, 20, and 30 mol%).

Table 4. Overview of measured lattice parameters and comparison between targeted and actual dopant concentration (Nd mol%) in sintered microspheres, prepared from a simplified infiltration process on 823 K calcined microspheres.

***T*cal (K)**	**Pore-former**	**Target χ(Nd) (mol%)**	**Lattice parameter *a* (Å)**	**Actual χ(Nd) (*mol*%)**
		0	5.4709(1)	-
		5	5.4687(1)	3.9(4)
823	none	10	5.4668(1)	6.8(4)
		20	5.4638(1)	14.0(4)
		30	5.4626(1)	16.4(4)

4. Discussion

The effect of calcination temperature and the use of pore-formers on microstructural parameters such as SSA, density and porosity were investigated in detail. A drastic effect of the calcination temperature was observed. Physically stable and porous uranium oxide microspheres could be obtained by limiting the calcination temperature to 773 K or 823 K, without requiring the need for a pore-former (see Table 1). At more elevated temperatures, the density of the microspheres increased substantially, and consequently, the porosity decreased. Katalenich *et al.* similarly reported the densification and SSA reduction with elevated temperatures between 723 K and 1023 K [43]. Likely, some coarsening effects set in which cause the U_3O_8 grains to interconnect.

In a second approach, the added effect of pore-formers mixed in the sol was investigated. It is recognized that compounds such as carbon black and graphite have also been used to increase the thermal properties of microspheres in some studies [19,21,44]. With respect to their effect on porosity, Förthmann and Blass showed that approximately 20% total porosity can be obtained in sintered UO_2 microspheres prepared *via* internal gelation, by addition of 60 g carbon per liter starting solution [45]. In this work, emphasis was on the microstructure after calcination, to promote infiltration, and it was found that the use of graphite as pore-former should be excluded because it requires an elevated calcination temperature (1073 K) to fully decompose, which negatively impacts the density and porosity (see Table 2). Similarly, the use of carbon black as a pore-former requires calcination temperatures up to 1073 K [17], which is too high to prepare porous uranium oxide microspheres.

To avoid excessively high calcination temperatures, starch was used instead of graphite or carbon black. Starch requires a significantly lower calcination temperature to fully decompose (793 K), in comparison to graphite or carbon black, and it was observed that the microstructural properties were not adversely affected. Although the SSA of the calcined microspheres prepared with starch were slightly lower than those fabricated without pore-former, the apparent density is similar after calcination at 823 K but with a considerable gain in the degree of accessible porosity. This was also confirmed by SEM observations (see Figure 5), evidencing the formation of macroporosity. After calcination at 773 K and without the use of starch, the UO_3 microsphere surface appears very smooth in contrast to the very rough and porous surface of the $UO_3 + U_3O_8$ microsphere calcined at 823 K. Likely, the spallation of U_3O_8 from UO_3 contributes to the surface roughness and increased SSA value. The starch doped microspheres calcined at 823 K (UO_3) also have a rather smooth surface, but have wider pores and isolated large macropores. The different morphology between both sets of microspheres calcined at 823 K is most likely related to the presence of U_3O_8 in microspheres prepared without starch.

A sub-set of three microsphere types which showed the most promising microstructural characteristics, *i.e.* uranium oxide microspheres without pore-former and calcined at 773 K or 823 K and with addition of starch as pore-former and calcined at 823 K, was selected to perform infiltration with Nd as a surrogate for Am. The methodology of the infiltration process was based on a review of the relevant literature and own exploratory work. As such, successive infiltrations were applied to reach dopant concentrations above 10 mol% (see also

Figure 1). The XRD patterns (see Figure 6) show that a single solid solution phase was obtained after sintering, *i.e.* no peak splitting was observed. The infiltration efficiency was evaluated from the lattice contraction after sintering (see Table 3) and it was observed that for dopant levels up to 10 mol%, all three microsphere routes performed equally well. Higher dopant concentrations (20 mol% and above) could only be reached with the microspheres calcined at 823 K, both with and without pore former. A comparison of the relevant microstructural parameters reported in Table 1 and Table 2 shows that the apparent density of all three microspheres types is very similar (59-65 % TD), but the SSA of microspheres calcined at 773 K (14.1 m^2/g) is significantly lower than that of microspheres calcined at 823 K with or without starch pore-former (24.7 and 18.9 m^2/g, respectively). Also, the use of starch as pore-former substantially increased the accessible porosity, but it gave only a small additional gain in Nd concentration (25.1 mol% instead of 23.7 mol%) for otherwise identical infiltration conditions (i.e. a target of 30 mol%). Likely, the effect of increased accessible porosity was offset by the decrease in SSA. An interesting observation was that these microspheres were much less brittle and did not deform during manipulation, as compared to their counterparts without pore former. In general, the usefulness of starch addition in the process will depend on the application: With the aim to produce spherical particle fuel, obtaining more physically stable kernels is beneficial, whereas if the infiltrated microspheres are compressed into pellets this feature is of less relevance.

The use of successive infiltration and re-calcination steps to reach higher dopant concentrations introduces some added complexity to the process flow sheet (see Figure 1). However, it avoids the preparation of more than two aliquots of the dopant solution. When handling aqueous feeds containing minor actinides this can be considered advantageous as it reduces losses and the risk for spills, while also limiting dose exposure times in batch experiments. On the other hand, a simplified, single step infiltration requires less process steps, but at the cost of additional manipulation of aqueous feeds (see Figure 8). In order to probe the effectiveness of both methods, the simplified infiltration process was also applied on 823 K calcined microspheres (without pore-former). The results presented in Table 4 showed that at the lower range of targeted concentration (up to 10 mol%) the actual dopant concentration was comparable to results on the other series, but significant deviation between targeted and actual Nd concentration occurred in the higher range (20 to 30 mol%). Small differences between target and actual concentrations are affected by the stochastic variation which includes errors in sampling, and concentration of the dopant solution. However, the large offsets observed here indicate an inefficient infiltration of the microspheres *via* the single step approach. Possible sources for the discrepancy are the formation of small Nd-rich clusters, or an asymmetrical concentration variation, which do not contribute significantly to the peak positions of the diffraction patterns. Additionally, a substantial amount of the dopant solution may have crystallized on the surface of the crucible, as the solution dries out and reaches the solubility limit before being impregnated entirely into the microspheres. Further research efforts and process optimization are required to find out if the simplified route can lead to equally good results.

5. Conclusion

The suitability of internal gelation to produce porous uranium oxide microspheres for subsequent doping *via* infiltration was explored, with the specific goal to achieve high dopant concentrations (up to 30 mol%). In a first part of the study, process conditions for the fabrication of porous microspheres were assessed. In all samples prepared without pore-former the calcination temperature showed an inverse relation to porosity and specific surface area. Ideal calcination temperatures for microspheres without pore-former were 773 K and 823 K. Also samples prepared with pore-formers showed the same inverse relation between calcination temperature and porosity or specific surface area. Microspheres containing graphite as pore-former required an elevated calcination temperature of 1073 K for complete decomposition of the pore-former, which resulted in little remaining porosity. The ideal calcination temperature for microspheres with starch as pore-former was 823 K.

In a second part of the study, infiltration, calcination and sintering was performed using neodymium nitrate solution as a surrogate for americium nitrate. A process involving successive infiltrations with intermittent calcination was applied for the highest target concentrations (20 and 30 mol%). While the infiltration efficiency was good for all microspheres with targeted Nd concentrations up to 10 mol%, one of the production routes without pore-former (i.e. using a calcination temperature of 773 K) underperformed at more elevated Nd concentrations. In the production routes where a calcination temperature of 823 K was applied (with and without pore-former) an effective concentration in the solid solution nearly identical to the target concentration of 20 mol% was obtained. For a target of 30 mol% the solid solution concentration was limited to around 25 mol%, with a minor improvement caused by the use of starch as pore-former.

Both with and without pore-formers, internal gelation combined with optimized calcination conditions offers thus a route for porous uranium oxide microspheres enabling infiltration and subsequent solid solution formation up to at least 20 mol% of Nd, and it may be expected that similar concentrations will be achievable also for Am. Although the use of starch as pore-former did not substantially improve the infiltration efficiency, a side observation was that it suppressed the formation of U_3O_8 at a calcination temperature of 823 K, and as a result these microspheres showed a better physical stability.

A simplified, single-step infiltration process was applied on one of the production routes. However, above targeted Nd concentrations of 10 mol% significant discrepancies with the effective concentration in the solid solution were observed. Further process optimization is required to find out if the simplified route can lead to equally good results at elevated target concentrations.

Supporting Information

X-ray diffractograms of sintered microspheres, prepared *via* infiltration.

CRediT author statement

Gamze Colak: Writing - original draft, writing - review & editing, conceptualization, methodology, validation, formal analysis, investigation, data curation, visualization. **Gregory Leinders:** Writing - original draft, writing - review & editing, methodology, validation, data curation, formal analysis, supervision, project administration. **Rémi Delville:** Writing - review & editing, supervision, project administration. **Frédéric Jutier:** Writing - review & editing, investigation, supervision. **Marc Verwerft:** Writing - review & editing, resources, supervision, funding acquisition. **Jef Vleugels**: Writing - review & editing, conceptualization, resources, supervision.

Acknowledgements

The authors gratefully acknowledge Dr. C. Schreinemachers for providing the ADUN solution used in this work, and for sharing expertise on the subject. G. Colak thanks K. Vanaken and P. Dries for laboratory assistance. Financial support for this research was provided by the Energietransitiefonds of the Belgian FPS Economy (project: ASOF – Advanced Separation for Optimal management of spent Fuel).

References

[1] J. Magill, V. Berthou, D. Haas, J. Galy, R. Schenkel, H.-W. Wiese, G. Heusener, J. Tommasi, G. Youinou, Nuclear Energy, (2003) 263.
[2] S. Pillon, J. Somers, S. Grandjean, J. Lacquement, Journal of Nuclear Materials, 320 (2003) 36.
[3] R.J.M. Konings, R. Conrad, G. Dassel, B.J. Pijlgroms, J. Somers, E. Toscano, Journal of Nuclear Materials, 282 (2000) 159.
[4] K. Tanaka, S. Miwa, S.-i. Sekine, H. Yoshimochi, H. Obayashi, S.-i. Koyama, Journal of Nuclear Materials, 440 (2013) 480.
[5] K. Richter, A. Fernandez, J. Somers, Journal of Nuclear Materials, 249 (1997) 121.
[6] D. Warin, F. Sudreau, S. Pillon, N. Drin, L. Donnet, E. Brunon, "The FUTURIX - transmutation experiment in Phenix", (2004).
[7] E. D'Agata, S. Knol, A. Fedorov, A. Fernandez, F. Klaassen, Journal of Nuclear Materials, 465 (2015).
[8] A. Fernández, D. Haas, R.J.M. Konings, J. Somers, Journal of the American Ceramic Society, 85 (2002) 694.
[9] D. Lundberg, I. Persson, Coordination Chemistry Reviews, 318 (2016) 131.
[10] T. Delahaye, F. Lebreton, D. Horlait, N. Herlet, P. Dehaudt, Journal of Nuclear Materials, 432 (2013) 305.
[11] E. Remy, S. Picart, T. Delahaye, I. Jobelin, F. Lebreton, D. Horlait, I. Bisel, P. Blanchart, A. Ayral, Journal of Nuclear Materials, 453 (2014) 214.
[12] L. Ramond, P. Coste, S. Picart, A. Gauthé, M. Bataillea, Journal of Nuclear Materials, 492 (2017) 97.
[13] S. Picart, *et al.*, "Porous metal oxide microspheres from ion exchange resin", 2015.
[14] Y. Croixmarie, E. Abonneau, A. Fernández, R.J.M. Konings, F. Desmoulière, L. Donnet, Journal of Nuclear Materials, 320 (2003) 11.
[15] M.A. Pouchon, G. Ledergerber, F. Ingold, K. Bakker, "3.11 - Sphere-Pac and VIPAC Fuel", in: R.J.M. Konings (Ed.) Comprehensive Nuclear Materials, Elsevier, Oxford, 2012, pp. 275-312.
[16] A. Fernandez, K. Richter, J. Somers, Journal of Alloys and Compounds, 271 (1998) 616.
[17] M. Couland, S. Fourcaudot, R. Jovani Abril, A. Fernandez-Carretero, J. Somers, Journal of the American Ceramic Society, 95 (2012) 133.
[18] M. Vespa, M. Rini, J. Spino, T. Vitova, J. Somers, Journal of Nuclear Materials, 421 (2012) 80.
[19] C. Nästrén, D. Staicu, J. Somers, A. Fernandez, Journal of Nuclear Materials, 433 (2013) 314.
[20] N. Boucharat, A. Fernandez, J. Somers, R.J.M. Konings, D. Haas, Progress in Nuclear Energy, 38 (2001) 255.
[21] C. Nästrén, A. Fernandéz-Carretero, J. Somers, Nuclear Technology, 181 (2013) 331.
[22] J. Somers, A. Fernández, Journal of the American Ceramic Society, 88 (2005) 827.
[23] J. Somers, A. Fernandez, Progress in Nuclear Energy, 48 (2006) 259.
[24] L.W. Chan, H.Y. Lee, P.W.S. Heng, Carbohydrate Polymers, 63 (2006) 176.
[25] E. D'Agata, *et al.*, Nuclear Engineering and Design, 275 (2014) 300.
[26] E. D'Agata, *et al.*, Nuclear Engineering and Design, 311 (2017) 131.
[27] S. Finkeldei, *et al.*, "Synthesis and Characterization of UO_2 Feedstocks containing Controlled Dopants, Report No. ORNL/SPR-2019/1067", (2019).
[28] C. Schreinemachers, G. Leinders, G. Modolo, M. Verwerft, K. Binnemans, T. Cardinaels, Nuclear Engineering and Technology, 52 (2020) 1013.
[29] J.L. Collins, M.H. Lloyd, R.L. Fellows, Radiochimica Acta, 42 (1987) 121.

[30] J. Härtwig, G. Hölzer, E. Förster, K. Goetz, K. Wokulska, J. Wolf, physica status solidi (a), 143 (1994) 23.
[31] S. Brunauer, P.H. Emmett, E. Teller, Journal of the American Chemical Society, 60 (1938) 309.
[32] J. Rouquerol, *et al.*, Pure and Applied Chemistry, 84 (2011) 107.
[33] B. Zhang, S.A. Davis, S. Mann, Chemistry of Materials, 14 (2002) 1369.
[34] K.S.W. Sing, Pure and Applied Chemistry, 57 (1985) 603.
[35] C. Schreinemachers, G. Leinders, G. Modolo, M. Verwerft, K. Binnemans, T. Cardinaels, Journal of Nuclear Materials, 535 (2020) 152128.
[36] S.M. Lee, T.W. Knight, S.L. Voit, R.I. Barabash, Nuclear Technology, 193 (2016) 287.
[37] J.-F. Wadier, "Diagramme de phases et propriétés thermodynamiques du système uranium-néodyme-oxygène", PhD thesis, Université de Paris VI (1973).
[38] T. Ohmichi, S. Fukushima, A. Maeda, H. Watanabe, Journal of Nuclear Materials, 102 (1981) 40.
[39] K. Une, M. Oguma, Journal of Nuclear Materials, 118 (1983) 189.
[40] C. Schreinemachers, A.A. Bukaemskiy, M. Klinkenberg, S. Neumeier, G. Modolo, D. Bosbach, Progress in Nuclear Energy, 72 (2014) 17.
[41] R. Bès, K. Kvashnina, A. Rossberg, G. Dottavio, L. Desgranges, Y. Pontillon, P.L. Solari, S.M. Butorin, P. Martin, Journal of Nuclear Materials, 507 (2018) 145.
[42] G. Leinders, T. Cardinaels, K. Binnemans, M. Verwerft, Journal of Nuclear Materials, 459 (2015) 135.
[43] J.A. Katalenich, B.B. Kitchen, Journal of Sol-Gel Science and Technology, 98 (2021) 288.
[44] R.D. Hunt, J.A. Johnson, J.L. Collins, J.W. McMurray, T.J. Reif, D.R. Brown, Journal of Nuclear Materials, 498 (2018) 269.
[45] R. Förthmann, G. Blass, Journal of Nuclear Materials, 47 (1973) 259.